Article:
Nanayakkara, M.P.A., Matjačić, L., Wood, S. et al. (2021) Ultra-low dark current organic–inorganic hybrid X-ray detectors. Advanced Functional Materials, 31 (8). 2008482. ISSN: 1616-301X

https://doi.org/10.1002/adfm.202008482

Ultra-low dark current organic-inorganic hybrid X-ray detectors via vertical composition gradient

M. P. A. Nanayakkara, L. Madjacic, S. Wood, F. Richheimer, S. Jenatsch, S. Zufle, R. Kilbride, A. J. Parnell, M. G. Masteghin, H.M. Thirimanne, A. Nisbet, K. D. G. I. Jayawardena, S. R. P. Silva

Abstract

Organic-inorganic hybrid semiconductors are an emerging class of materials for direct conversion X-ray detection due to attractive characteristics such as high sensitivity and the potential to form conformal detectors. However, existing hybrid semiconductor X-ray detectors display dark currents that are significantly higher than industrially accepted values of 1-10 pA mm^{-2}. Herein, we report ultra-low dark currents of <10 pA mm^{-2} , under reverse bias voltages as high as -200 V, for these hybrid X-ray detectors through enrichment of the hole selective p-type organic semiconductor near the anode contact. The resulting detectors demonstrate broadband X-ray response including an exceptionally high sensitivity of ~1.5 mC Gy^{-1} cm^{-2} and <6% variation in angular dependence response under 6 MV hard X-rays. The above characteristics in combination with excellent dose linearity, dose rate linearity, and reproducibility over a broad energy range enable these detectors to be developed for medical and industrial applications.

Introduction

Optoelectronic devices based on organic semiconductors are gaining significant attention, due to the possibility of fabricating detectors whose response that can be tuned over a broad

energy range on flexible architectures that can be manufactured using low-cost roll-to-roll and sheet-to-sheet printing techniques[1–3]. Recently, the use of these devices has been expanded for X-ray detection, with the potential for a wide range of applications including medical diagnostics, industrial inspection, and scientific research (e.g. crystallography)[4–8]. Strategies used for the adoption of organic semiconductors for X-ray detection include the incorporation of high-atomic number (Z) elements into the semiconductor structure[9] and the incorporation of high-Z direct converting nanoparticles (NPs)[10–12] or scintillators[13] into an organic bulk heterojunction (BHJ) matrix. In particular, the direct conversion X-ray detection strategy developed by Thirimanne et al.[14], where high atomic number bismuth oxide (Bi_2O_3) nanoparticles were incorporated into an organic BHJ consisting of p-type Poly(3-hexylthiophene-2,5-diyl) (P3HT) and n-type [6,6]-Phenyl C71 butyric acid methyl ester ($PC_{70}BM$), demonstrated appealing characteristics such as low voltage operation and high sensitivity over a broadband energy range. The concept was further expanded by Jayawardena et al.[15] to demonstrate X-ray imaging.

Despite the promise shown by the above NP incorporated BHJ (NP-BHJ) direct conversion X-ray detectors, they suffer from high dark currents of $\sim 10^4$ pA mm^{-2} under an applied bias of -10 V (equivalent to an electric field of $\sim$0.3 V μm^{-1}). This value is well above the dark current values of 10 pA mm^{-2} exhibited by state-of-the-art X-ray detectors[16]. As low dark currents are an important metric that enable the detection of low doses and a good dynamic range[17], it is important to develop routes to minimize dark currents in these hybrid detectors.

One possible reason behind this adverse performance is the poor charge selectivity at the device contacts. The use of poly(3,4-ethylenedioxythiophene): poly(styrene sulfonate) (PEDOT: PSS) as the hole transport layer (HTL) is known to result in poor charge selectivity in organic photovoltaics and photodetectors[18–20]. Additionally, the hygroscopic nature of PEDOT: PSS results in the corrosion of indium tin oxide (ITO) leading to fast degradation of the devices[21–23]. This has led to the investigation of alternative transport layers based on transition metal oxides such as Molybdenum oxide (MoO_x)[24–26], and Nickel oxide (NiO)[27] in combination with inverted device architectures.

Here, we report a route towards achieving ultra-low dark currents that are below 10 pA mm^{-2}, even at high electric fields of $\sim$4 V μm^{-1} in HTL free, inverted NP-BHJ direct conversion X-ray detectors. These values, to the best of our knowledge are the lowest dark currents reported thus far for organic or hybrid X-ray detectors (**Figure 1a**). We demonstrate the

formation of a vertical composition gradient within the active layer leading to the enrichment of the p-type P3HT semiconductor near the anode contact. This enrichment results in X-ray detectors with acceptable performance, even without the addition of an external HTL. The resulting detectors demonstrate broadband response with sensitivities of ~60 nC Gy^{-1} cm^{-2} under 70 kV X-ray irradiation and a remarkably high sensitivity of around ~1.5 mC Gy^{-1} cm^{-2} under 6 MV photon irradiation from a medical linear accelerator. Furthermore, these NP-BHJ detectors with low dark currents demonstrate excellent dose linearity and dose rate linearity, reproducibility, and low beam incidence angle dependence. Such features enable these detectors to be well suited commercially for imaging and dosimetry in medical and industrial applications.

Results

Response characteristics of the NP-BHJ X-ray detectors

The organic-inorganic hybrid X-ray absorber consists of high-Z direct converting Bi_2O_3 NPs as the X-ray absorber, while the P3HT and $PC_{70}BM$ form percolation pathways for extraction of holes and electrons (respectively) (**Figure 1b, c**). The X-ray detectors were fabricated by adopting an inverted device architecture where the NP-BHJ composite was sandwiched between ITO and silver (Ag) electrodes (**Figure 1d**) resulting in a glass/ITO/zinc oxide/NP-BHJ/HTL/Ag architecture, enabling both electron and hole extraction (**Figure 1e**). Using thermogravimetric analysis (TGA), the NP loading in the film (by weight) was estimated to be 38.1% which is slightly higher than the NP loading in the starting ink (33.3 %). This is

attributed to the use of non-functionalised NPs which can lead to some variation in the NP distribution within the ink. The thickness of the NP-BHJ film was around 55 µm.

Fig. 1 Organic-inorganic hybrid X-ray detectors enabling ultra-low dark currents. a Comparison of the

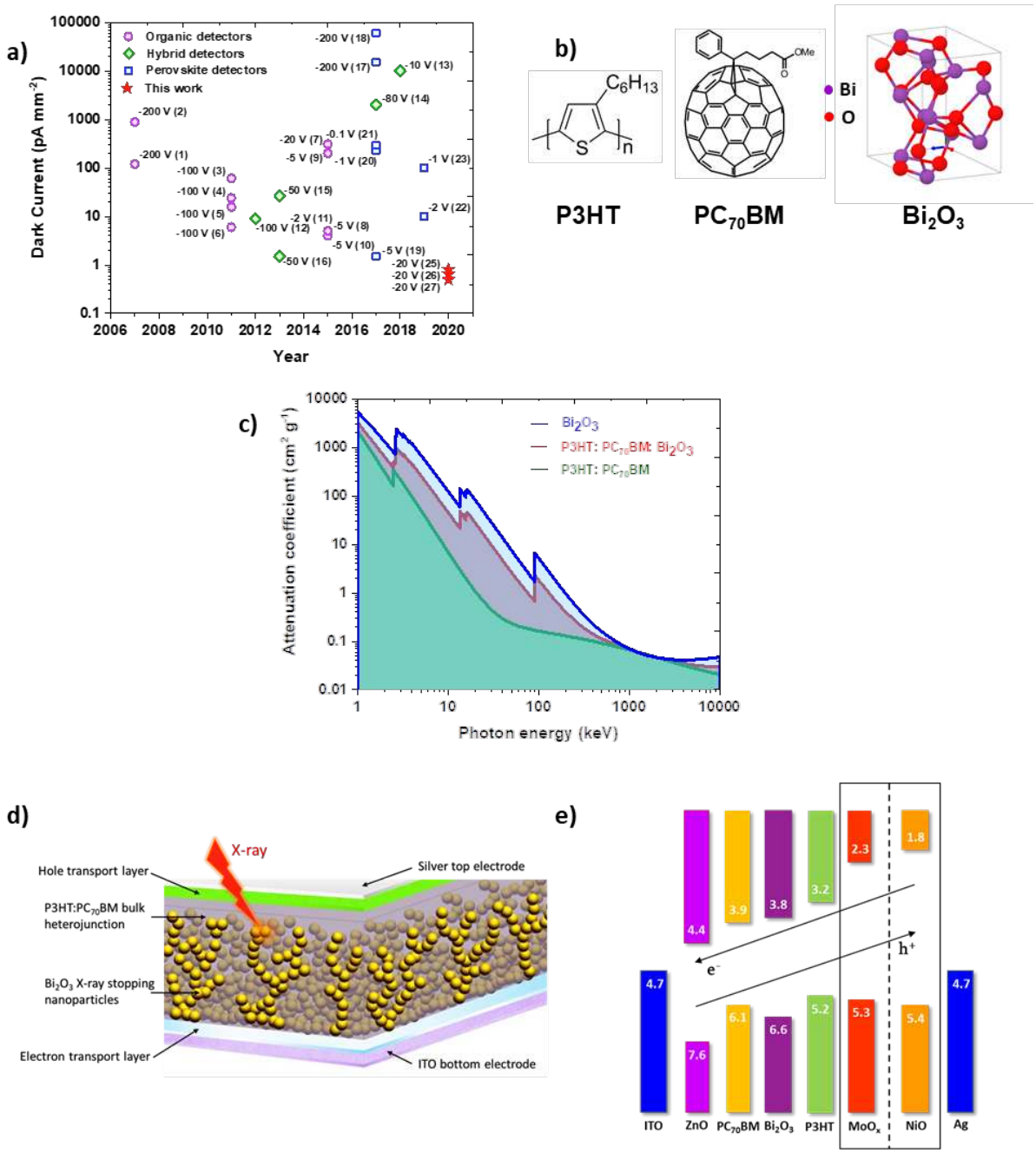

dark current response characteristics of the recently developed organic and organic-inorganic hybrid direct conversion X-ray detectors. (1)-(2)[2], (3)-(6)[28], (7)[29], (8)-(10)[30], and (11)[31] are organic X-ray detectors, (12)[11], (13)[14], (14)[10], (15)-(16)[12] are organic-inorganic hybrid X-ray detectors fabricated by incorporating high-Z NPs, (17)[32], (18)[33], (19)[5], (20)-(21)[6], (22)[34], and (23)[35] are perovskite based X-ray detectors ,and (25), (26), and (27) are the X-ray detectors developed in this work. The operating voltage is given adjacent to each data point. **b** Chemical structure of P3HT, $PC_{70}BM$, and Bi_2O_3. **c** Comparison of the mass attenuation coefficient of Bi_2O_3 NPs, organic BHJ consisting of P3HT and $PC_{70}BM$, and the P3HT: Bi_2O_3: $PC_{70}BM$ blend indicating the enhancement of X-ray attenuation by incorporation of high-Z NPs. **d** Schematic of the NP-BHJ X-ray detector architecture used in this work. **e** Flat band diagram for the device architecture used in this work. All energy

values are given in eV. Energy values for P3HT, Bi_2O_3, and $PC_{70}BM$ are from reference[15], for MoO_x from reference[24,26], for NiO and ITO from reference[27], and for Ag from reference[36].

Initially, we investigated the influence of NiO as an HTL, on the X-ray detector characteristics of the NP-BHJ system. The NiO layer was deposited using a NP ink which enables compatibility with printing techniques. The surface roughness induced by the topographical features of the active layer, or by the addition of a transport layer, has a significant influence on the detector response characteristics.[37] A lower surface roughness is required to minimize dark injection currents resulting from field enhancement effects as described by Fowler-Nordheim emission[38]. In order to identify the optimum NiO layer thickness that minimizes leakage currents as well as undesired recombination losses within the HTL, we studied the influence of the NiO coating thickness. This was achieved by controlling the NiO NP concentration in the ink from 2.5, 1.25, 0.63, 0.31, to 0.16 wt.%. Hereafter the detectors with 2.5, 1.25, 0.63, 0.31, and 0.16 wt.% of NiO concentrations are referred to as "NiO 2.5", "NiO 1.25", "NiO 0.63", "NiO 0.31", and "NiO 0.16" detectors, respectively. The resulting NiO film thicknesses are given in **Supplementary Figure 2**. Atomic force microscopy (AFM) was conducted on the NiO/NP-BHJ films (**Figure 2**) which indicated no notable variation in the surface roughness despite the variation in NiO concentration. The root mean square (RMS) roughness values obtained for the hybrid film with or without NiO coatings are summarized in **Supplementary Table 1**.

Fig. 2 Effect of NiO concentration on the surface roughness of the hybrid film. AFM micrographs of the organic-inorganic hybrid layer, **a** without NiO coating. When spin coated with **b** 2.5 wt. %, **c** 1.25 wt.%, **d** 0.63 wt.%, **e** 0.31 wt.%, and **f** 0.16 wt.% NiO dispersion. No significant variation in the root mean square surface roughness was observed irrespective of the HTL thickness.

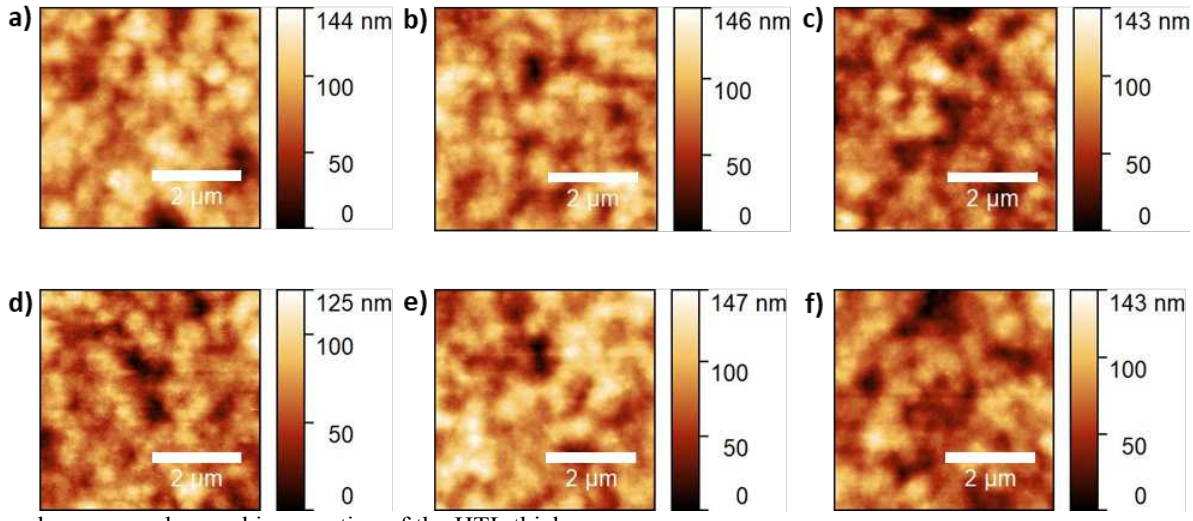

The temporal variation of the dark current of the X-ray detectors was evaluated under applied biases ranging from -10 V to -200 V, equivalent to macroscopic electric fields in the range of

~0.2 V μm^{-1} to ~4 V μm^{-1}. Following a sharp transient decay, the detectors displayed a stabilized dark current response, which is less than the industrially accepted limit of 10 pA mm^{-2}, irrespective of the voltage applied (**Supplementary Figure 3**). Furthermore, NiO-based detectors displayed no significant deviation of dark current response with the varying NiO concentration as shown in the **Figure 3a**. These findings are in agreement with the lack of variation in surface roughness with the NiO concentration as discussed previously.

The X-ray photocurrent response from the detectors was studied by exposure to X-rays generated from a 70 kV X-ray source. The source-to-detector distance was maintained at 20 cm. As the BHJ used here is sensitive to the visible portion of the electromagnetic spectrum, all measurements were conducted under dark conditions to eliminate the effects from stray light. Upon X-ray exposure, the detectors displayed a "box shaped" X-ray photocurrent response with a sharp rise and decay (**Figure 3b**). This is contrary to the saw-tooth shaped transient photocurrent response reported for a number of organic semiconductor-based X-ray detectors where either proper charge selection layers were not incorporated[15,39] or, PEDOT: PSS was used as the HTL in combination with a conventional device architecture[14]. The observation of saw-tooth shaped characteristics has been attributed to the photoconductive gain mechanisms in mono-carrier type devices[39]. Therefore, it is evident that optimization of the interfaces provides a pathway towards improving device response time. Upon exposure to several doses under a constant dose rate and an applied bias, the detectors displayed a linear relationship between charge density and dose (**Figure 3c**). The sensitivity (S) of an X-ray detector, defined as the collected charge per unit area per unit exposure of radiation (given by equation(1) below) is an important device metric[40].

$$S = \frac{Q}{DA} = \frac{\int (I_{X-ray}(t) - I_{Dark})dt}{DA} \quad (1)$$

where, Q represents the charge generated under irradiation, I_{X-ray} and I_{Dark} represent the current under X-ray irradiation and in the dark, respectively, D is the X-ray incident dose, and A is the active area of the detector. Materials with high sensitivity are highly preferred for X-ray detection as they allow the detection of very small X-ray doses, thereby reducing the risks associated with ionizing radiation[41]. One possible way of estimating the sensitivity of an X-ray detector is based on the slope of the charge density vs. dose curve. Based on this method, the sensitivity of the NiO-based detectors was estimated to be in the range of 23.1-24.9 nC Gy^{-1} cm^{-2} at -10 V and 60-62 nC Gy^{-1} cm^{-2} at -200 V. It should be noted that the sensitivity was observed to be independent of the NiO concentration. Furthermore, dose rate dependence

analysis on the detectors indicated linear behaviour between the X-ray photocurrent density and the dose rate, as shown in **Figure 3d.** The slope of the photocurrent density with respect to the dose rate provides another means of estimating the sensitivity;

$$S = \frac{I}{D_R A} = \frac{I_{X-ray} - I_{Dark}}{D_R A} \quad (2)$$

where, D_R is the incident X-ray dose rate. Based on the dose rate dependence method, sensitivities in the range of 20.7-22.1 nC Gy^{-1} cm^{-2} (at -10 V) was estimated for the NiO-based detectors, similar to that estimated from the slope of the charge density vs. dose curve. We further studied the reproducibility of the detector response characteristics through exposure to ten consecutive X-ray pulses (**Figure 3e**). The reproducibility of the photocurrent response of each detector was quantitatively assessed by normalizing the charge extracted under each exposure to that of the initial exposure. This analysis indicated the maximum deviation of each detector response was less than 3.5 %, indicating a very good reproducibility due to minimal charge trapping effects. The mobility-lifetime ($\mu\tau$) constant is a key metric used in comparing the charge transport properties in semiconductors used for X-ray detection. The relationship between the $\mu\tau$ constant, applied voltage and the collected charge is described by the Hecht equation[42] given below;

$$Q = Q_O \frac{\mu\tau V}{d^2}\left[1 - \exp\left(-\frac{d^2}{\mu\tau V}\right)\right] \quad (3)$$

where, Q is the total charge extracted, Q_O the asymptotic charge, V the applied voltage, d the detector thickness, μ the charge carrier mobility, and τ the charge carrier lifetime. To evaluate the $\mu\tau$ constant for the NP-BHJ detector studied here, the voltage dependence of the X-ray photocurrent response of the detectors was studied from -10 V to -200 V under a constant dose and dose rate. The curve was fitted with the Hecht relationship (**Figure 3f** and **Supplementary Figure 4**) which showed that the $\mu\tau$ product of the detectors is $\sim 10^{-7}$ cm^2 V^{-1}. These results are within an order of magnitude of the values reported for thick NP-BHJ X-ray photoconductors ($\sim 1.7 \times 10^{-6}$ cm^2 V^{-1})[15] and stabilized a-Se photoconductors (2×10^{-6} to 2×10^{-5} cm^2 V^{-1})[43]. Moreover, the signal to noise ratio (SNR) (evaluated as the ratio between the photocurrent density and dark current density) of the detectors was evaluated as a function of applied voltage as shown in **Figure 3g**. The SNR of the detectors displayed a decaying characteristic due to the increase in dark current with voltage (**Figure 3h**) as opposed to the Hecht-type relationship observed for the X-ray photocurrent which saturates at

high voltages. The high SNR at low operating voltages indicates the potential of these detectors for low power sensing applications, such as wearable dosimeters.

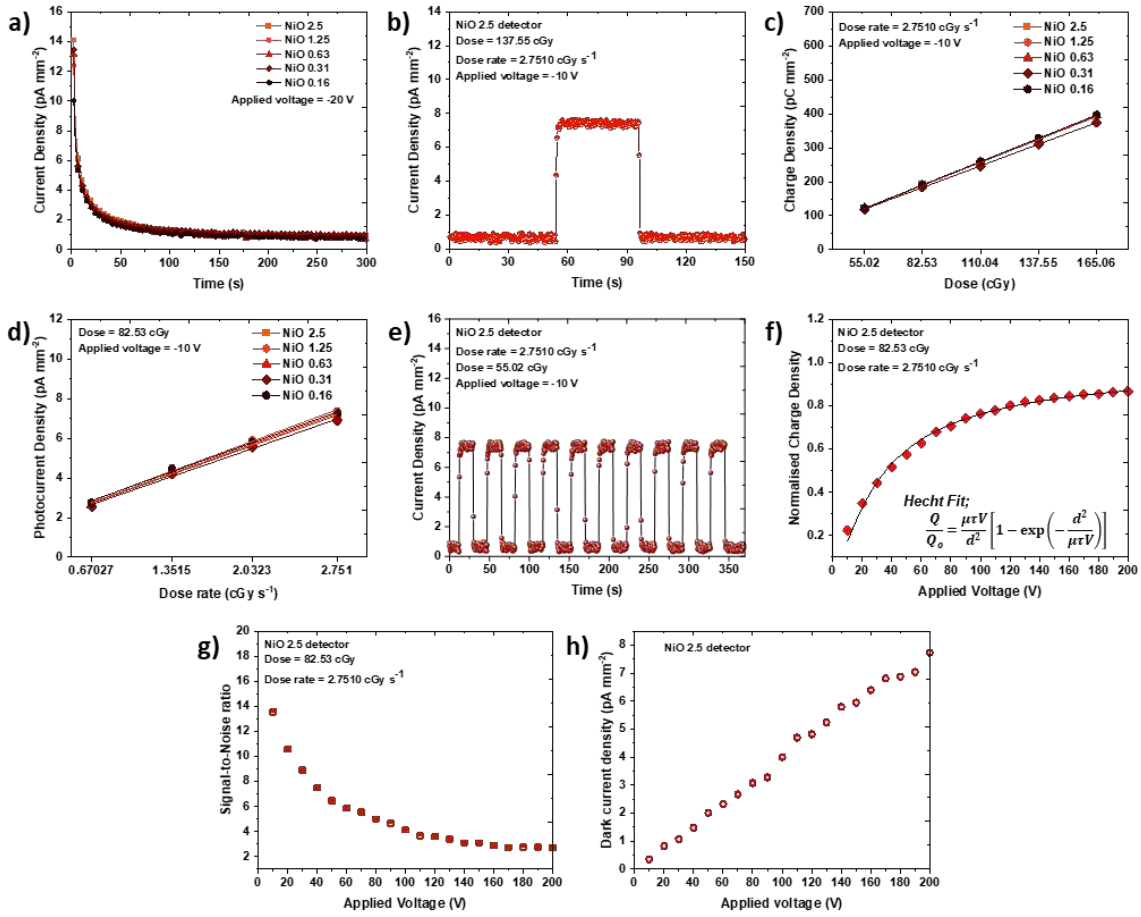

Fig. 3 Response characteristics of the NiO-based detectors under 70 kV X-rays. a Dark current variation as a function of time. The dark currents saturate at a value ~0.8 pA mm^{-2}. **b** Transient X-ray photocurrent response from the NiO 2.5 detector indicating a "box-shaped" response. **c** Dose and, **d** Dose rate dependence for the NiO-based detectors. The solid lines indicate linear fits. Both the dose as well as dose rate dependence shows excellent linearity ($R^2 > 0.9998$). **e** Reproducibility of the X-ray photocurrent response of the NiO 2.5 detector under repeated X-ray exposures. **f** Voltage dependence of the NiO 2.5 detector together with the Hecht fit ($R^2 > 0.9998$) for estimation of the μτ product. **g** SNR variation with applied bias of the NiO 2.5 detector. **h** Dark current variation as a function of applied bias of the NiO 2.5 detector indicating the nearly linear relationship between the dark current and the applied bias. Data points in **Figures c, d, f, g, h** are averaged over three measurements.

We also evaluated the detector performance by replacing the NiO HTL with a 10 nm thick thermally evaporated MoO_x film as the HTL (hereafter MoO_x detectors) (**Supplementary Figure 5**). These MoO_x detectors displayed stable yet very low dark current response of approximately 0.5 pA mm^{-2} (at -20 V), together with a sensitivity value of 22.6 nC Gy^{-1} cm^{-2} (at -10 V), similar to the sensitivities of the NiO-based detectors.

In the above study, the variation of the NiO thickness was not observed to result in any significant variation in the detector performance, even under very low NiO NP concentrations (resulting in a ~7 nm thick HTL layer). As this points towards the possible formation of a

charge selective layer within the NP-BHJ film itself, we evaluated the characteristics of detectors without any additional HTL layers (hereafter "HTL Free" detectors). Despite the absence of an external HTL, these detectors also displayed a stable and ultra-low dark current response of ~0.65 pA mm^{-2} at -20 V (**Figure 4a**) and ~5.44 pA mm^{-2} at -200 V. Similar to the devices incorporating NiO as an HTL, the HTL Free devices demonstrated a "box-shaped" X-ray photocurrent response (**Figure 4b**). The detectors also demonstrate excellent dose linearity (**Figure 4c**) and dose rate linearity (**Figure 4d)** resulting in sensitivity values of 24.2 and 20.4 nC Gy^{-1} cm^{-2} (at -10 V) (respectively) which are comparable to the sensitivities observed from NiO-based detectors. The HTL Free detectors also demonstrated a reproducible X-ray photocurrent response (**Figure 4e**) with a maximum deviation less than 2.3%. Furthermore, Hecht analysis carried out on the HTL Free detectors (**Figure 4f**) results in a $\mu\tau$ value in the range of 10^{-7} cm^2 V^{-1}. The SNR of HTL Free detectors displayed a decaying characteristic (**Figure 4g**) due to the increase in dark current with voltage (**Figure 4h**), similar to that observed for devices incorporating an HTL. This is again attributed to the linear increase in dark current with voltage as opposed to the saturation in X-ray photocarriers extracted with increasing voltage. For each type of detector, the sensitivity at -10 V (estimated from the dose dependence and dose rate dependence method), the $\mu\tau$ product, SNR at -20 V, and maximum deviation observed in the reproducibility analysis are summarized in **Supplementary Table 2**.

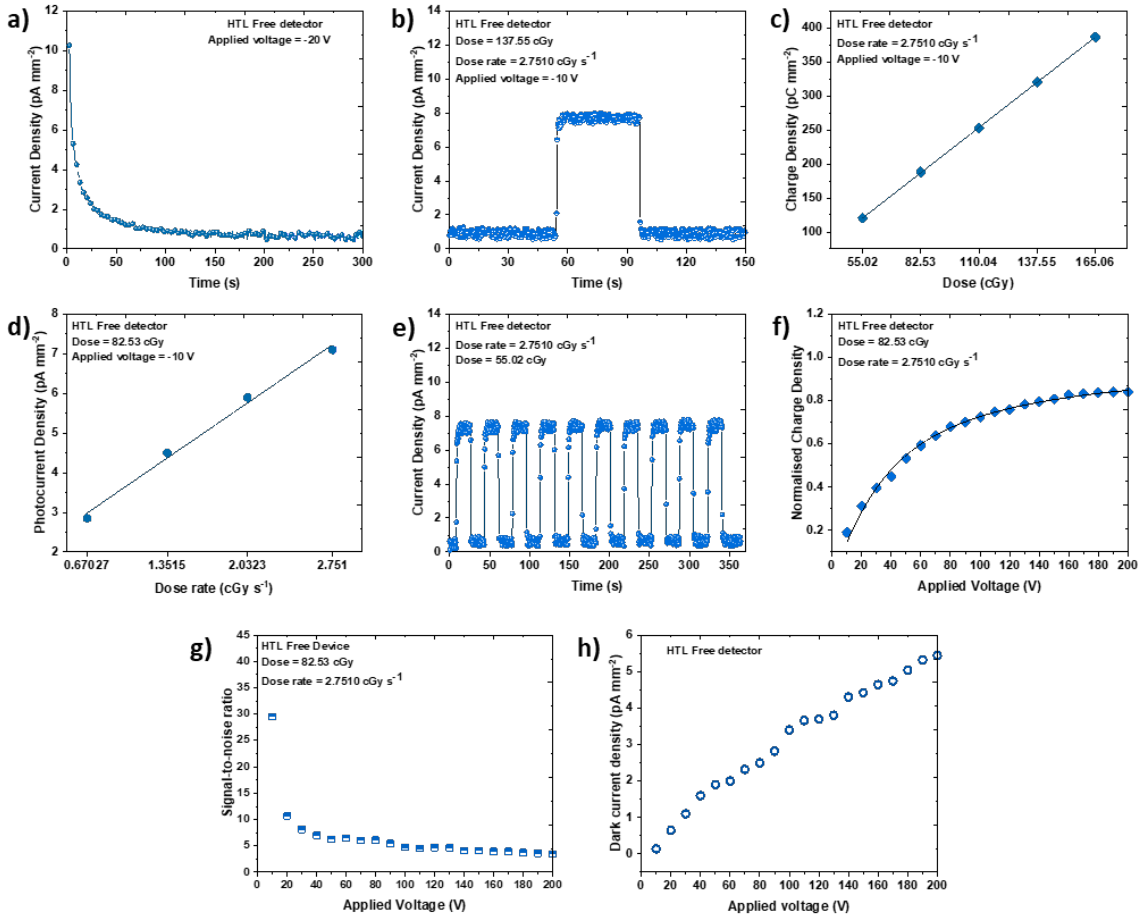

Fig. 4 Response characteristics of the HTL Free detector under 70 kV X-rays. a Dark current variation as a function of time. The dark currents saturate at a value around 0.65 pA mm^{-2}. **b** Transient X-ray photocurrent response from the HTL Free detector indicating a "box-shaped" response. **c** Dose and, **d** Dose rate dependence for the HTL Free detector. The solid lines indicate linear fits. Both the dose as well as dose rate dependence shows excellent linearity ($R^2 > 0.9998$). **e** Reproducibility of the X-ray photocurrent response of the HTL Free detector under repeated X-ray exposures. **f** Voltage dependence of the detector together with the Hecht fit ($R^2 > 0.9998$) for estimation of the μτ product. **g** SNR variation with applied bias and **h** Dark current variation as a function of applied bias of the HTL Free detector. A drop in SNR is observed due to increase in the dark current and saturation of the X-ray photocurrent with increasing voltage. Data points in **Figures c**, **d**, **f**, **g**, **h** are averaged over three measurements.

Formation of a charge selective layer within the NP-BHJ films

Based on the detector response characteristics observed under 70 kV soft X-ray radiation, it is evident that the HTL Free detectors are capable of generating a performance that is similar to detectors with an HTL. This indicates the formation of an internal hole selective/electron blocking layer closer to the anode contact. As stated previously, in the NP-BHJ detector concept, the two organic semiconductors P3HT and $PC_{70}BM$ are used to achieve efficient transport of holes and electrons (respectively) generated within the Bi_2O_3 NPs upon X-ray attenuation. The efficient extraction of charge is expected to be enabled through the formation of a three-dimensional bi-continuous percolating network, similar to that found within organic photovoltaics. However, it is possible that the solvent annealing step used in

NP-BHJ film formation may have resulted in a phase-separation process leading to the segregation of the p-type P3HT component near the anode contact. Firstly, we carried out scanning Kelvin probe microscopy (SKPM) in order to identify the nature of the electronic contact formed between the NP-BHJ surface and the silver contact. SKPM measurements carried out (**Figure 5a**) indicate the average surface potential of the hybrid layer to be approximately 4.6 eV. The near similarity of this surface potential to the work function of silver (4.7 eV)[36] is likely to facilitate the formation of an ohmic contact between the silver anode and the hybrid layer.

In order to further understand the compositional gradient within the NP-BHJ films, we carried out cross-sectional analysis (**Figure 5b**) using a Xenon Plasma focused ion beam–scanning electron microscope (FIB-SEM) Dual Beam system. We observed the sedimentation of a majority of the Bi_2O_3 NPs (green false coloured) at the bottom of the hybrid film (i.e. closer to the electron transport layer), resulting in an organic-semiconductor rich capping layer. **Supplementary Figure 6** shows a backscattered (BSE-SEM) image of a larger cross-section of the sample, in which the prominent contrast between the brighter heavy NPs and the lighter organic active region is highlighted.

To identify the vertical chemical compositional profile of the NP-BHJ film and the composition of this capping layer, we carried out Time-of-Flight Secondary Ion Mass Spectroscopy (ToF-SIMS) analysis (**Figure 5c**). To better preserve the molecular information, an Ar cluster ($Ar^+_{1700-2000}$) ion source was used[44] in this study to achieve gentle erosion throughout the entire thickness of the film. **Figure 5d** illustrates the 3D renderings which describe the distribution of the negative ion species (X=Y=50 μm, Z~55 μm) of interest across the film. It can be seen that the S^- (sulphur) signal, due to the presence of P3HT is the strongest, and uniform throughout the thickness, whereas the C_{70}^- signal due to $PC_{70}BM$ and the $Bi_2O_3^-$ signal due to Bi_2O_3 NPs appears to be confined to the bottom of the film. This verifies our hypothesis on the enrichment of the p-type P3HT species near the top surface (**Figure 5e**), which can act as an efficient electron blocking/hole selective layer within the device architecture studied here. Similar segregation of P3HT in P3HT: PCBM BHJ solar cells has been reported by several authors[45,46]. The formation of such phase-separation and the enrichment of the p-type organic semiconductor is attributed to minimization of the surface energy of the final film formed. Previous reports indicate that fullerene derivatives (e.g. PCBM) possess high surface energies (e.g. 38.2 mN m^{-1})[47] in comparison to organic semiconductors such as Poly(9,9-dioctylfluorene-alt-benzothiadiazole)

(32.2 mN m^{-1})[47] or P3HT (19.8 mN m^{-1})[48]. The lower surface energy of the p-type semiconductor results in its preferential accumulation at the free surface of the film, which results in the minimization of the film surface energy. This energy minimization process, which also results in expellin PCBM from the polymer domains,[46] is influenced by additional processing parameters such as thermal annealing time period[49–51], P3HT molecular weight and regioregularity[52], and incorporation of additives[53,54]. We note that the beneficial impact of such phase segregation process has also been utilized in increasing the power conversion efficiency of organic solar cells[45,46].

Fig. 5 Vertical phase separation within the hybrid film. a SKPM micrograph of the top surface of the hybrid film indicating an average surface potential of 4.6 eV, similar to the work function of the anode contact. **b** Cross-sectional micrograph (false coloured) of the hybrid film depicting the sedimentation of Bi_2O_3 NPs to the bottom interface of the hybrid film leaving behind an organic rich top layer. The green color clusters represent the Bi_2O_3 NP aggregates while the red color regions represent the organic content. **c** Depth profile of the hybrid film obtained from ToF-SIMS depicting the distribution of ion species S^-, C_{70}^-, and $Bi_2O_3^-$ along the film depth. **d** 3D renderings of the negative polarity data (X=Y=50 μm, Z~55 μm) obtained from ToF-SIMS for the S^-, C_{70}^-, and $Bi_2O_3^-$ ions showing the P3HT enrichment at the top surface of the hybrid layer. **e** Schematic of the organic-inorganic hybrid film illustrating the vertical composition gradient resulting in a P3HT rich top region and an organic–inorganic mixed bottom region.

In order to further understand the nature of crystallization of the P3HT enriched phase, we

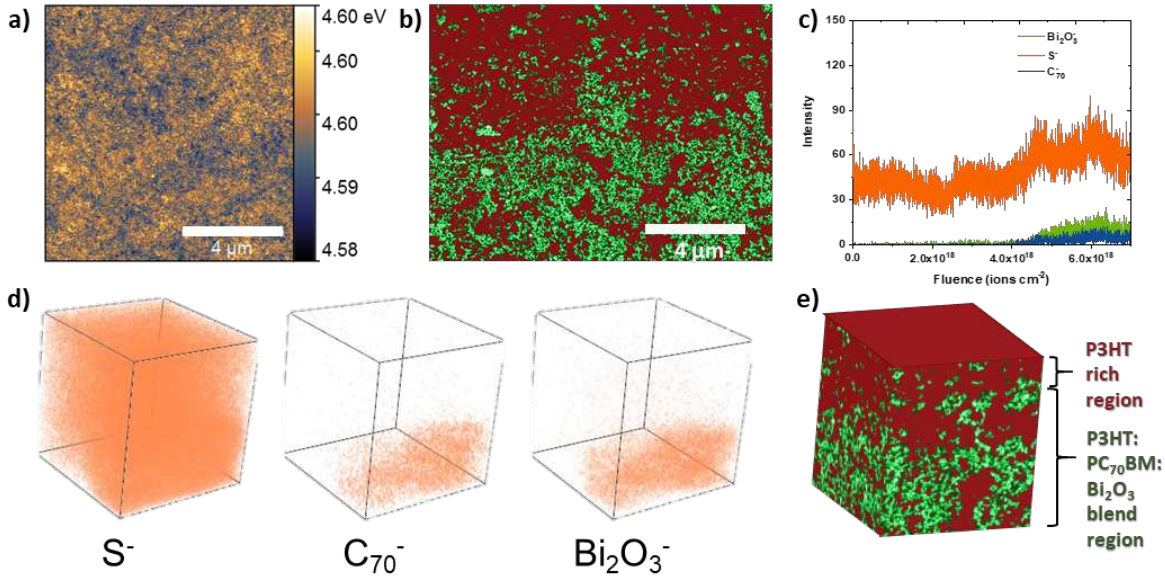

conducted grazing incidence wide-angle X-ray scattering (GIWAXS) on the NP-BHJ films. Below the critical angle ($\alpha_c \approx 0.12°$), X-rays travel as an evanescent plane wave along the sample surface probing the near surface features of the film (the top $\sim 10\ nm$) whereas angles above the critical angle give information about the bulk of the film[55]. Therefore, during this study GIWAXS spectra were acquired at incident angles 0.05° and 0.1°($\alpha_i < \alpha_c$), as well as 0.2° and 0.3° ($\alpha_i > \alpha_c$) to enable probing of the sub-surface as well as the "bulk" region (up

to $\sim 2\mu m$ depth). When used in organic photovoltaic devices, the high temperature (140℃) annealing step has been reported to be a critical factor for P3HT phase segregation[46,56]. Since the film formation is carried out under an initial low temperature (60℃) "solvent annealing" step followed by a high temperature (140℃) annealing step, GIWAXS spectra were obtained for films that have undergone both annealing steps (hereafter "annealed sample") and only the initial low-temperature solvent annealing step (hereafter "unannealed sample"). The 2D GIWAXS images acquired under each incident angle for both unannealed and annealed samples are illustrated in **Figure 6**. For both unannealed and annealed samples, there is a narrow peak at $Q_z \sim 0.4$ Å^{-1} corresponding to the (100) lamellar stacking of P3HT polymeric chains[57], indicating that the P3HT phase has already crystallized during the low-temperature solvent annealing step. Furthermore, based on the higher intensity of the P3HT (100) peak along the Q_z axis, it is evident that the P3HT crystallites formed in the NP-BHJ film have predominantly adopted edge-on orientation where π-π stacking is in the plane of the film and alkyl side chains are perpendicular to the substrate[58]. Since charge transport is more efficient along the main chain and π-π stacking direction while side chains act as charge barriers, edge-on orientation is high desirable compared to face-on orientation[59]. The average P3HT crystallite size for the unannealed and annealed samples were calculated using the Scherrer formula[60] (equation(4)) on the P3HT (100) peak in the 1D radial integration plots (**Figure 6i** and **6j**).

$$D = \frac{K\lambda}{\beta Cos\theta} \tag{4}$$

Here, D is the crystallite size, K is the dimensionless shape factor (0.94), λ is the X-ray wavelength (0.134 nm), β is the full width at half maximum (FWHM) of the P3HT (100) peak in radians, and θ is the Bragg angle in radians. The FWHM was estimated by Gaussian fitting of the P3HT (100) peak for each incident angle (**Supplementary Figure 7**). An increase in the P3HT crystallite size was observed after the high temperature annealing step. For example, at an incident angle of 0.05°, the crystallite size of P3HT was estimated to be 14.1 nm for the unannealed sample which was observed to increase to 14.7 nm following the high temperature annealing step (**Supplementary Table 3**).

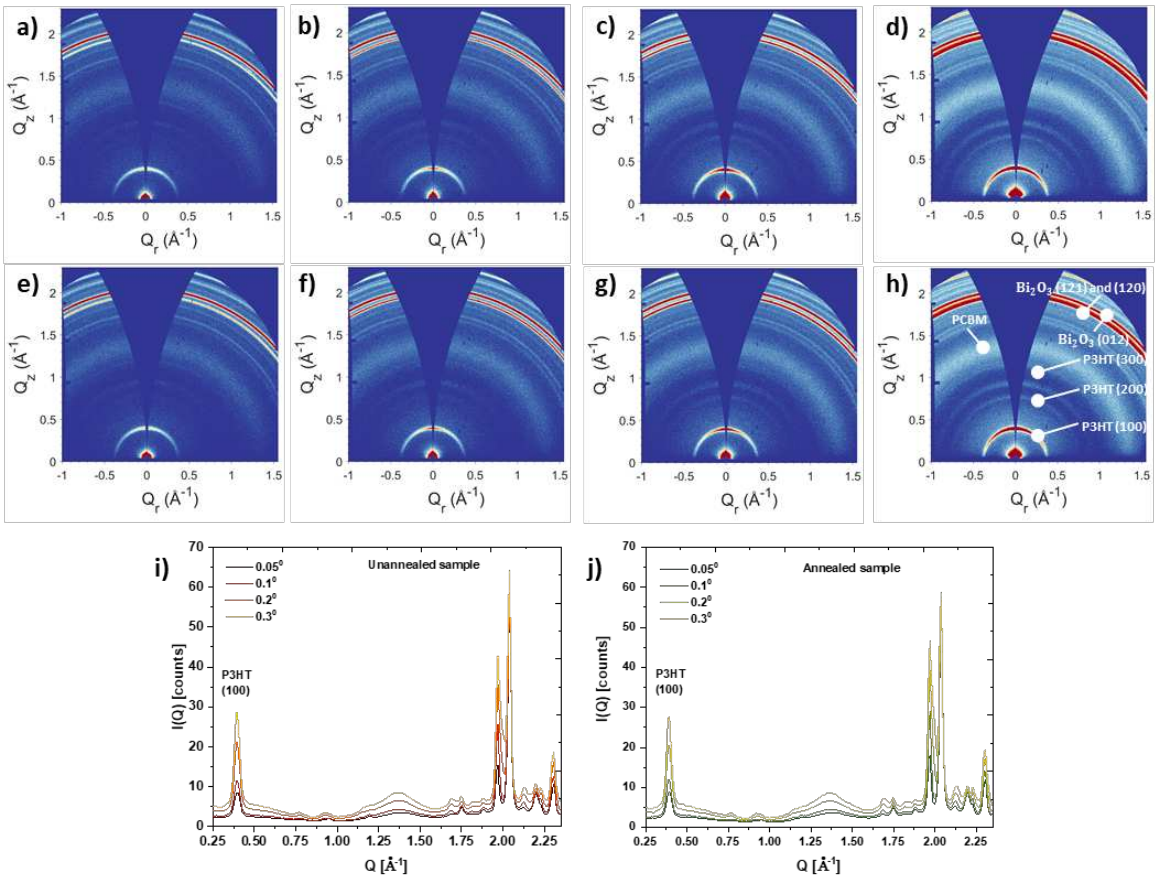

Fig. 6 Crystallization within the segregated P3HT phase. 2D GIWAXS spectra for the unannealed NP-BHJ film obtained at **a**. 0.05°, **b**. 0.1°, **c**. 0.2°, and **d**. 0.3° incident angles, and for the annealed NP-BHJ film at **e**. 0.05°, **f**. 0.1°, **g**. 0.2°, and **h**. 0.3° incident angles indicating the increase of the (100) peak signal at $Q_z \sim 0.4$ Å^{-1} with depth. Indexing for peaks corresponding to P3HT, PCBM, Bi_2O_3 are displayed in panel **h**. 1D radial integrations of the **i.** Unannealed NP-BHJ film and **j.** Annealed NP-BHJ film for various incidence angles. A decrease in peak widths with increasing incidence angle is observed, indicating the increase in P3HT crystallite size.

Overall, the ToF-SIMS and GIWAXS spectra measurements indicate a semi-crystalline P3HT rich capping layer in the NP-BHJ film. This P3HT-rich capping layer (which forms an ohmic contact with the metal anode) acts as a charge selective layer that results in the ultra-low dark currents observed for the HTL free hybrid X-ray detectors.

Charge transport characteristics of the NP-BHJ X-ray detectors

Following the identification of the vertical phase segregation that takes place within the NP-BHJ layer, we proceeded to study the charge transport properties of the system that was facilitated by the organic semiconductors used. The charge carrier mobility of the NP-BHJ detectors was estimated using the "photo-charge carrier extraction by linearly increasing voltage" (photo-CELIV) method. We note that the broadband nature of the illumination source which extends to ~700 nm enables generation of excitons at the absorption edge of P3HT. As the absorption coefficient of P3HT significantly decreases at its absorption edge, this enables photo-carrier generation throughout the thickness of the NP-BHJ layer (**Supplementary Figure 8**). The detectors were illuminated under 475 W m^{-2} white LED light for 1000 μs and the photo-CELIV measurements were conducted under several ramp rates/ voltage rise speeds. **Figure 7a** displays the photo-charge extraction transient recorded for the HTL Free detector under a ramp rate of 1 V ms^{-1}. The photo-CELIV charge carrier mobility was estimated from the equation[61] given below;

$$\mu = \frac{2d^2}{3At_{max}^2\left[1+0.36\frac{Jmax-Jo}{Jo}\right]} \quad (5)$$

Where, μ is the charge carrier mobility, d is the detector active layer thickness, A is the ramp rate, J_{max} is the peak current, and J_o is the current plateau value at the end of the ramp. For the HTL Free detector, estimated carrier mobilities were in the range of 10^{-4} cm^2 V^{-1} s^{-1} to 10^{-3} cm^2 V^{-1} s^{-1} resulting in a mean mobility value of 2.85×10^{-4} cm^2 V^{-1} s^{-1}. Other detectors tested in this work also displayed a mobility value of similar magnitude (**Supplementary Figure 9**). These mobility values are in the same order as those reported for the previous generation of NP-BHJ X-ray detectors (~10^{-3} cm^2 V^{-1} s^{-1})[14] estimated from the Time-of-flight method as well as those reported for the P3HT: $PC_{70}BM$ organic BHJ solar cells (6.4×10^{-4} cm^2 V^{-1})[62] estimated from the photo-CELIV method. While the photo-CELIV technique does not enable mobilities of electrons and holes to be extracted separately, the characteristic t_{max} depends predominantly on charge carrier with the higher mobility[63]. However, the "box shaped" nature of the X-ray photocurrent transients observed (as opposed to a saw-tooth profile) indicates that the charge carriers possess nearly similar mobilities.

The charge carrier recombination lifetime of the detectors was estimated by conducting impedance spectroscopy (IS) (i.e. under dark conditions). The impedance spectra were acquired under four negative applied bias conditions (0, -1, -2, -4 V). **Figure 7b** shows the

Nyquist plots for the HTL Free detector biased under the above-mentioned voltages where two semicircles are observed; one at high frequencies above 15 kHz (**Figure 7c**) and the other one at lower frequencies below 15 kHz. Similar behaviour was observed for devices comprising NiO and MoO_x as the HTL (**Supplementary Figure 10**). The Nyquist plots were analysed using an equivalent circuit shown in the **inset of Figure 7b**, consisting of R_1 and R_2 resistance components which form a parallel circuit with constant phase elements, CPE_1 and CPE_2. We attribute one semicircle to the top surface of the hybrid film which is enriched with P3HT phase while the other semicircle to the bottom region of the film consisting of Bi_2O_3 NPs, P3HT, and $PC_{70}BM$[64,65]. The adopted circuit model can describe the impedance characteristics accurately since the simulated curves[66,67] match well with the impedance spectra across the whole frequency range. Furthermore, from the impedance spectra, two characteristic times associated with charge carrier transport can be extracted. The effective charge carrier lifetime (τ_n) from the peak position of the larger semicircle in the low frequency regime. Also the charge carrier transit time (τ_d), from the transition point of the first semicircle to the second semicircle[68]. From the impedance spectra recorded at -2 and -4 V, we estimated the carrier lifetime to be in the range of ~3 to 13 ms for each detector, irrespective of the hole selective condition. To evaluate the influence of an increased carrier density on the recombination lifetimes, we carried out intensity modulated photovoltage spectroscopy (IMVS) measurements. The recombination lifetimes estimated from the IMVS technique (**Figure 7d** and **Supplementary Figure 11**) was estimated to be between ~50 μs and 70 μs which is two orders of magnitude lower than that estimated using IS. This is in agreement with increased charge carrier recombination in the presence of a higher carrier density.

We further evaluated the response speed of the NP-BHJ detectors based on the rise time (time taken to achieve 63% of the saturated photocurrent signal) and decay time (time taken to achieve 37% of the saturated photocurrent signal) of the X-ray detectors as a function of applied bias by using the transient photocurrent (TPC) method. Each detector was illuminated with a 475 W m^{-2} white LED light for a duration of 500 μs and the photocurrent responses were recorded at biases ranging from -5 to -10 V. The photocurrent transients reported under each bias condition for the HTL Free detector are shown in **Figure 7e**. The photocurrent transients of the NP-BHJ X-ray detectors demonstrated rise time and decay time components in the microsecond time scales unlike the box shaped photocurrent transient observed during the X-ray photocurrent measurements. However, it should be noted that the

rise time and decay times under our X-ray irradiation studies are masked by several factors including the settling time of the X-ray source (usually a few seconds), and the limitations of the readout electronics used. This is contrary to the measurement setup used for TPC, which allowed observation of the photocurrent on microsecond scale. We observed that for each detector, the rise time does not change significantly with increasing negative applied bias, whereas the decay time of the detectors reduced with the increasing negative applied bias (**Figure 7f** and **Supplementary Figure 12**). This relationship between the decay time and the applied bias can be attributed to the field dependence of the charge carrier mobility in organic semiconductors leading to increased charge carrier extraction under higher electric fields[69]. Overall, the rise times of the NiO-based detectors were ~23-24 μs whereas HTL Free detectors showed a rise time of ~29 μs. Furthermore, the decay time of the HTL Free detectors was approximately 50 μs when an applied bias of -10 V was applied. Such decay times are comparable to that of the high purity Germanium detectors which have been reported to display decay times in the order of 10 μs[70]. The relatively fast response times of the optimized NP-BHJ detectors indicate that very low trap states exist at the electrode/interlayer/NP-BHJ interface and that any bulk traps existing within the organic-inorganic hybrid layer are relatively shallow[32].

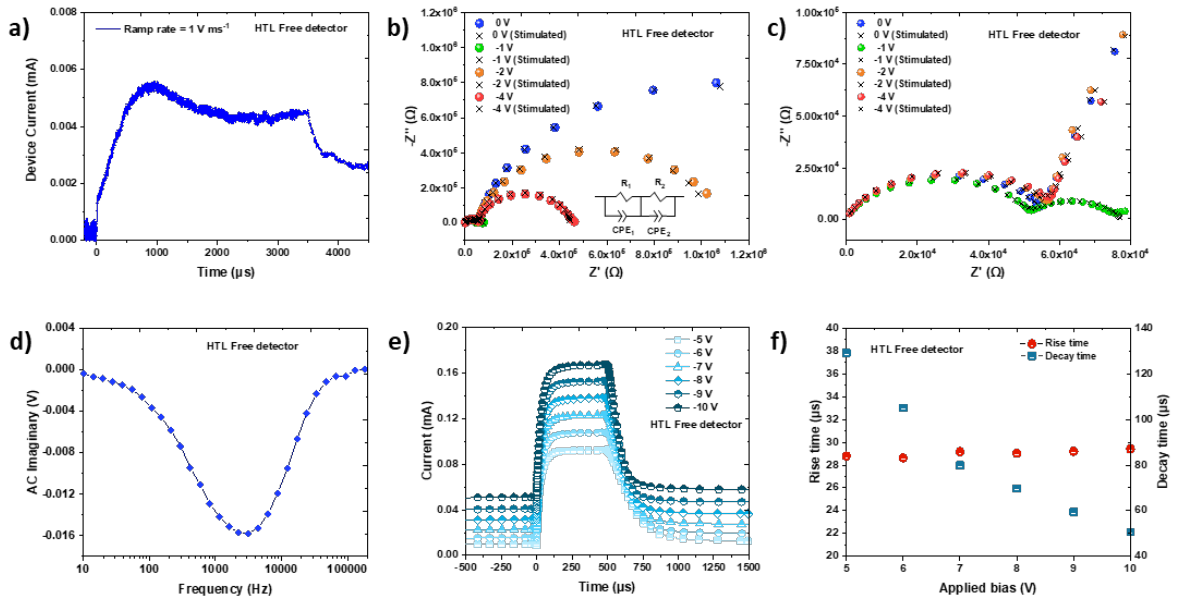

Fig. 7 Charge carrier transport in NP-BHJ X-ray detectors. a Example photocurrent transient as a function of delay time of the HTL Free detector measured using the photo-CELIV technique. **b** Nyquist plots for the HTL Free detector obtained under dark conditions when biased at 0, -1, -2, and -4 V. The black color crosses (×) represent the fits for each bias calculated using the equivalent circuit shown in the inset. The R_1 and R_2 are resistance components forming a parallel circuit with the constant phase elements CPE_1 and CPE_2. **c** An expanded view of the Nyquist plots of the HTL Free detector displaying the smaller semicircle at frequencies above 15 kHz. **d** IMVS spectrum of the HTL Free detector from which, recombination lifetimes in the range of ~50 µs and 70 µs are estimated. **e** Photocurrent transients of the HTL Free detector under -5, -6, -7, -8, -9, and -

10 V biases**. f** Rise time of the HTL Free detector plotted together with decay time, both as a function of applied bias. The decay time reduces with increasing voltage which is attributed to the field dependent mobility of carriers in organic semiconductors.

Dosimetric characterization of NP-BHJ X-ray detectors for radiotherapy

One possible application of these NP-BHJ X-ray detectors would be as a dosimeter for dose mapping during radiotherapy. Conventional radiotherapy techniques such as Intensity Modulated Radiotherapy (IMRT) and Volumetric Modulated Arch Therapy (VMAT) require precise dosimeters to accurately monitor incident dose, exit dose and dose distributions during verification measurements to confirm accuracy of radiotherapy treatment delivery[71–73]. Therefore, during this study we conducted a preliminary evaluation to assess the potential of our low dark current HTL Free hybrid detectors to function as dosimeters. The detector performance was investigated under exposure to hard X-rays from a 6 MV clinical linear accelerator (**Figure 8a** and **8b**) under an applied bias of -100 V. Analogous to the response characteristics observed under 70 kV X-ray radiation, we observed a sharp rise and decay in X-ray photocurrent response with a "box shaped" photo transient (**Figure 8c**). The HTL Free detectors also displayed an excellent dose linearity and dose rate linearity as shown in the **Figure 8d** and **8e**, respectively. The sensitivity of the detector estimated from the dose dependence method was ~1.5 mC Gy^{-1} cm^{-2} which is approximately six orders of magnitude greater than the sensitivity observed under 70 kV X-ray radiation. This increased sensitivity is attributed to the higher dose, applied bias, and the X-ray energy applied to this detector. Even though the expected X-ray attenuation is poor at high energies, it should be noted that Compton scattering becomes dominant in this energy range, therefore resulting in an electron cascade contributing towards a very high sensitivity[74]. Furthermore, this sensitivity value is substantially higher compared to the previous generation of NP-BHJ detectors (~60 μC Gy^{-1} cm^{-2})[14] and polycrystalline diamond detectors (~0.7 μC Gy^{-1} cm^{-2}) [75], both characterized under 6 MV X-rays. The detectors also displayed very high reproducibility under the repeated X-ray exposures, with a maximum deviation of only 2.8% as shown in **Figure 8f**. The voltage dependence of the HTL Free detectors under hard X-ray radiation was studied by applying a bias ranging from -5 V to -100 V. The trend between the charge density and applied voltage was fitted to the Hecht equation (**Figure 8g**) yielding a $\mu\tau$ product of approximately 1.806×10^{-7} cm^2 V^{-1} which is comparable to the result obtained from the voltage dependence studies under 70 kV soft X-ray radiation.

During IMRT and VMAT, the gantry head of the linear accelerator is rotated around the body for the beam delivery from specific angles to the target volume consisting of the tumour and

appropriate margin to account for possible microscopic spread and geometric uncertainties arising from internal patient motion and patient set up[73]. Therefore, in such a scenario, a dosimeter must be able to accurately measure the dose irrespective of the beam angle/gantry angle. In order to evaluate the angular dependence of the detector response, we carried out X-ray photocurrent measurements by varying the gantry angle of the linear accelerator from -90° to +90° (**Figure 8h**). We observed a slight dependence of the photocurrent response of the detector on the beam angle, particularly at intermediate angles between 0° and ±90°. The quantitative analysis of the normalized charge density generated at each angle to the charge density at 0^0 indicates a maximum deviation of 5.6 % (at +60°) (**Figure 8i**). However, this

value is significantly lower compared to the angular dependencies reported from commercial diode detectors which showed a maximum deviation of about 21 %[76,77].

Fig. 8 Response characteristics of the HTL Free detector under the 6 MV Hard X-rays. a Schematic of the

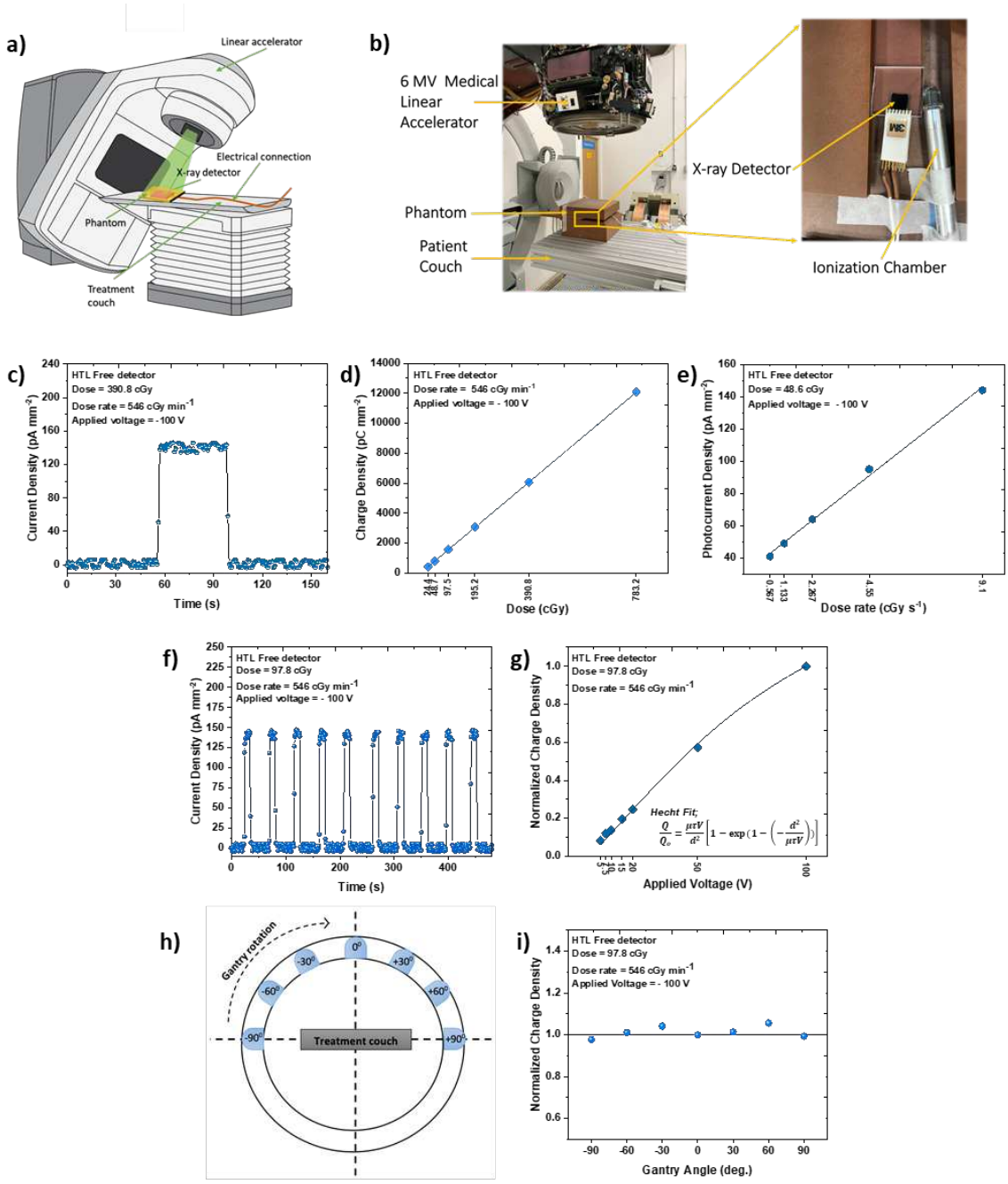

experimental arrangement used for detector characterization under 6 MV hard X-ray radiation. **b** An enlarged view of the experimental arrangement emphasizing the configuration of the detector, ionization chamber and the phantom. **c** X-ray photocurrent response from the detector. **d** Dose and, **e** Dose rate dependence of the HTL Free detector showing excellent linearity ($R^2 > 0.9998$). **f** Reproducibility of the response characteristics under repeated X-ray exposure. **g** Voltage dependence of the detector together with the Hecht fit ($R^2 > 0.9998$) for estimation of the μτ product.. **h** Schematic diagram illustrating the gantry angle rotation of the linear accelerator. **I** Beam angle dependence of the detector showing less than 6% variation in detector response with beam incidence angle. Data points in Figures **c**, **d**, **e**, **g**, **i** are averaged over three measurements.

Discussion

We have developed HTL Free organic-inorganic hybrid X-ray detectors with ultra-low dark currents below 10 pA mm^{-2} under electric fields as high as ~4 V μm^{-1}. This was identified to be due to the vertical phase separation induced within the BHJ thereby resulting in an internal hole selective mechanism. Such X-ray detectors fabricated without an HTL displayed very appealing characteristics such as dose linearity, dose rate linearity, and reproducibility not only under 70 kV soft X-ray radiation but also under 6 MV hard X-ray radiation with an exceptionally high sensitivity of ~1.5 mC Gy^{-1} cm^{-2}. The above-mentioned characteristics combined with the ultra-low dark currents, high sensitivity, and low beam angle dependence indicate that these detectors are promising candidates for dosimetry in radiotherapy, medical imaging as well as industrial applications. Therefore, if properly engineered for optimized charge transport within the active matrix, we can soon expect detector response characteristics comparable to the conventional X-ray detectors with added benefits of flexibility and much lower cost. This would stimulate further interest towards NP-BHJ composites for X-ray detection in a diverse range of applications including in remote areas with lower resources and power budgets.

Methods

Materials. Regioregular Poly(3-hexylthiophene-2,5-diyl) (P3HT; 80 mg; MW 46 kDa; Regioregularity 91%; Rieke 4002-EE), [6,6]-Phenyl C71 butyric acid methyl ester ($PC_{70}BM$; 80 mg; purity > 99%; Solenne), and Bi_2O_3 NPs (80 mg; β phase with a tetragonal crystal structure; 38 nm diameter; surface area 18 m^2 g^{-1}; Alfa Aesar) were added to Dichlorobenzene (DCB; 1 ml; anhydrous; Sigma-Aldrich) and stirred overnight to produce P3HT: $PC_{70}BM$: Bi_2O_3 solution. The solution was preheated at 60 □ while stirring for 30 min before deposition of the films. The solution preparation was carried out in a N_2 glove box (MBraun MB20G).

Device fabrication. Devices were fabricated on ITO (In_2O_3: Sn) glass substrates (15 mm × 15 mm, 15 Ω per square, Luminescence Technology Corp.). An electron transporting Aluminium-doped Zinc Oxide (ZnO) NP dispersion (Sigma-Aldrich) layer was spin coated in air (3000 rpm for 30 s) and annealed at 80℃ for 10 min to give a thickness of 40 nm. P3HT: $PC_{70}BM$: Bi_2O_3 solution was then casted. Devices were annealed (at 60℃) for ~60 min in air, until a relatively dry layer was obtained. After the low temperature annealing process, devices were annealed at 140℃ for 10 min in a N_2 glove box (MBraun MB20G). Devices were kept under vacuum at a pressure of less than 3 × 10^{-3} mbar for 48 h to remove any

residual solvent. This was followed by deposition of the hole transport layer; for NiO-based devices, each concentration of NiO (2.5, 1.25, 0.63, 0.31, and 0.16 wt. % in Ethanol; Avantama) was spin coated in air (at 1500 rpm for 30 s). For MoO_x devices, 10 nm thick MoO_x layer was thermally evaporated. For HTL Free devices, no external HTL was deposited. This was followed by the deposition of the silver anode (~120 nm) by thermal evaporation.

X-ray irradiation and characterization. For each detector, three measurements were recorded under each irradiation condition. Detector response was characterized under both soft and hard X-ray radiation;

1. A 70 kV microfocus X-ray source (Hamamatsu L6732-01) under a dose rate range of 0.67027 – 2.7510 cGy s^{-1}. A Keithley 2410 source measurement unit was used for recording the electrical characteristics.
2. 6 MV X-rays from a clinical linear accelerator (Elekta Synergy) located at the National Physical Laboratory (NPL). Dose rates from 34 cGy min^{-1} to 546 cGy min^{-1} were provided by the LINAC and a Keithley 2400 source measurement unit was used for recording electrical characteristics of the devices.

TGA. Thermogravimetric analysis of the NP-BHJ film was carried out under air, using a thermogravimetric analyzer (Q500 V6.7; TA Instruments). The sample was heated from room temperature to 700 □ at a heating rate of 10 □ min^{-1}.

Stylus profilometry. NiO (2.5, 1.25, 0.63, 0.31, and 0.16 wt. %) was spin coated on ITO coated glass substrates as stated earlier. The thickness achieved under each concentration of NiO was evaluated by Stylus Profilometry (Dektak XT; Bruker) using a 2 μm radius tip with a 2 mg stylus load.

AFM. Glass/ITO/NP-BHJ/NiO samples were prepared as stated earlier. The surface roughness of each NiO coated hybrid film was evaluated by using an AIST-NT atomic force microscope. The experiment was conducted in the tapping mode. The RMS roughness of the films was evaluated using the Gwyddion software.

SKPM. Glass/ITO/NP-BHJ samples were prepared as stated earlier. The surface potential of the NP-BHJ film was evaluated by amplitude-modulated 2-pass scanning Kelvin probe microscopy (Combiscope 1000; AIST-NT). The work function of the tip was calibrated on highly ordered pyrolytic graphite (HOPG) before and after the measurement on the hybrid

film to account for drift due to adsorbed water. The measurements were conducted in dry nitrogen, with oxygen and water below 1 ppm.

FIB-SEM. Samples were prepared by fabrication of the NP-BHJ film on the ITO coated glass substrates as described earlier. Cross sectional morphology of the NP-BHJ film was examined using a FERA3; TESCAN dual beam/focused ion beam scanning electron microscope under an accelerating voltage of 5 kV.

ToF-SIMS. Glass/ITO/NP-BHJ samples were prepared as stated earlier. Depth profiling of NP-BHJ film was performed with a TOF.SIMS 5 (IONTOF GmbH) time-of-flight secondary ion mass spectroscope using a 30 keV Bi_3^+ ions for analysis and $Ar_{(1700\text{-}2000)}^+$ ions at 20 keV for sputtering in non-interlaced mode. Low-energy electrons were used to flood the surface during the measurements. The sputter beam was rasterised in random mode over a 250 × 250 μm^2 area with the analysis area of 50 × 50 μm^2. Every plane of the analysed volume was rasterised in random mode with 128 × 128 pixels at 1 shot per pixel and 3 frames following by 7 frames of sputtering. The instrument was operated in the negative ion polarity.

Data acquisition was obtained using SurfaceLab software (IONTOF GmbH). Depth profiles were exported using the ASCII export function and 3D maps were exported using the 3D Rendering function.

GIWAXS. Samples were prepared by fabricating the NP-BHJ film on the ITO coated glass substrates where "Unannealed samples" were subjected only to low temperature solvent annealing step while the "Annealed samples" have undergone both low temperature and high temperature annealing steps. GIWAXS measurements were performed using a Xeuss 2.0 (Xenocs, France) system equipped with a liquid gallium MetalJet source (Excillum, Sweden) which provides a 9.243 keV X-ray beam. The beam was collimated to a spot of with a lateral dimension of 400 μm on the sample. A Pilatus3R 1M 2D detector (Dectris, Switzerland) placed at ~307 mm from the sample was used to obtain the diffraction images with both the sample chamber and flight tubes held under vacuum to remove background air scatter. Calibration of the sample-to-detector distance was carried out using a silver behenate calibrant in transmission geometry, while GIWAXS measurements were performed at incident angles of 0.05°, 0.1°, 0.2°, and 0.3°. This data was corrected, reduced and reshaped using the GIXSGUI MATLAB toolbox[78].

Parameters for the Scherrer formula were extracted from Gaussian curve fittings of the P3HT (100) peak using OriginPro software.

Photo-CELIV, IS, IMVS, and TPC. The Photo-CELIV, impedance spectroscopy, intensity modulated photovoltage spectroscopy, and transient photocurrent measurements were conducted using the Paios all-in-one test platform by FLUXiM. Devices were fabricated using the same methodology described for X-ray response characterization. The pixel area was reduced to 3 mm^2 in order to minimize capacitive effects that can influence device characteristics.

Acknowledgements

M.P.A.N., H.M.T. K.D.G.I.J., and S.R.P.S. gratefully acknowledge support from SilverRay Ltd. and EPSRC for this work ((EP/R025304/1). M.P.A.N. Acknowledges support from Advanced Technology Institute & DoC-CAT studentship, University of Surrey. K.D.G.I.J. acknowledges support from the Equality Foundation of Hong Kong. The GIWAXS measurements were carried out using the Sheffield Xeuss 2.0 SAXS instrument, A.J.P. and R. K. are grateful to Xenocs for their ongoing help and support in the user program at the University of Sheffield. We thank Philip Evans, G. Bass, J. Manning, and M. Homer of National Physical Laboratory (NPL) for their assistance with the LINAC measurements. We also thank V. Doucova (University of Surrey) for assistance with the TGA measurements.

Author information

Department of Electrical and Electronic Engineering, Advanced Technology Institute, University of Surrey, Guildford, Surrey, GU2 7XH, UK

M.P.A. Nanayakkara, M. G. Masteghin, H. M. Thirimanne, K. D. G. I. Jayawardena & S. R. P. Silva

National Physical Laboratory, Teddington, Middlesex, TW11 0LW, UK

L. Madjacic, S. Wood & F. Richheimer, A. Nisbet

FLUXiM AG, Katharina-Sulzer-Platz 2, 8400 Winterthur, Switzerland

S. Jenatsch & S. Zufle

Department of Physics and Astronomy, University of Sheffield, Hicks Building, Sheffield, S3 7RH, UK

R. Kilbride & A. J. Parnell

Department of Medical Physics and Biomedical Engineering, University College London, Gower St, Bloomsbury, London WC1E 6BT, UK

A. Nisbet

Corresponding author

Correspondence to S. R. P. Silva.

Email: s.silva@surrey.ac.uk

References

1. Diao, Y. *et al.* Solution coating of large-area organic semiconductor thin films with aligned single-crystalline domains. *Nat. Mater.* **12**, 665–671 (2013).
2. Boroumand, F. A. *et al.* Direct x-ray detection with conjugated polymer devices. (2007) doi:10.1063/1.2748337.
3. Arias, A. C., MacKenzie, J. D., McCulloch, I., Rivnay, J. & Salleo, A. Materials and Applications for Large Area Electronics: Solution-Based Approaches. *Chem. Rev.* **110**, 3–24 (2010).
4. Wei, H., Fang, H.-H. & Wang, C. Sensitive X-ray detectors made of methylammonium lead tribromide perovskite single crystals Hy-SPOD View project High Performance Radiation Detector, Photodetector and Solar Cells View project. (2016) doi:10.1038/nphoton.2016.41.
5. Pan, W. *et al.* Cs2AgBiBr6 single-crystal X-ray detectors with a low detection limit. *Nat. Photonics* **11**, 726–732 (2017).
6. Wei, W. *et al.* Monolithic integration of hybrid perovskite single crystals with heterogenous substrate for highly sensitive X-ray imaging. *Nat. Photonics* **11**, 315–321 (2017).
7. Gill, H. S. *et al.* Flexible perovskite based X-ray detectors for dose monitoring in medical imaging applications. *Phys. Med.* **5**, 20–23 (2018).
8. Yakunin, S. *et al.* Detection of X-ray photons by solution-processed organic-inorganic perovskites. doi:10.1038/nphoton.2015.82.
9. Ciavatti, A. *et al.* Boosting Direct X□Ray Detection in Organic Thin Films by Small Molecules Tailoring. *Adv. Funct. Mater.* **29**, 1806119 (2019).
10. Dynamics of direct X-ray detection processes in high-Z Bi2O3 nanoparticles-loaded PFO polymer-based diodes. doi:10.1063/1.4986345.
11. Intaniwet, A., Mills, C. A., Shkunov, M., Sellin, P. J. & Keddie, J. L. *High-Z nanoparticles for enhanced sensitivity in semiconducting polymer X-ray detectors*. *Nanotechnology* vol. 23 http://epubs.surrey.ac.uk/605295/4/Lohstroh_high-Z.pdf (2012).
12. Mills, C. A. *et al. Enhanced x-ray detection sensitivity in semiconducting polymer diodes containing metallic nanoparticles*. *J. Phys. D: Appl. Phys* vol. 46 http://epubs.surrey.ac.uk/787061/3/Mills_et_al_J_Phys_D_submission_after_referees_comments_FINAL_SRI.pdf (2013).
13. Büchele, P. *et al.* X-ray imaging with scintillator-sensitized hybrid organic photodetectors. *Nat. Photonics* **9**, 843–848 (2015).
14. Thirimanne, H. M. *et al.* High sensitivity organic inorganic hybrid X-ray detectors with direct transduction and broadband response. doi:10.1038/s41467-018-05301-6.
15. Jayawardena, K. D. G. I. *et al.* Millimeter-Scale Unipolar Transport in High Sensitivity

OrganicInorganic Semiconductor X-ray Detectors. *ACS Nano* **13**, 6973–6981 (2019).

16. Frey, J. B. *et al.* Dark current in multilayer stabilized amorphous selenium based photoconductive x-ray detectors. *J. Appl. Phys.* **112**, (2012).

17. Wronski, M. M. *et al.* A solid□state amorphous selenium avalanche technology for low photon flux imaging applications. *Med. Phys.* **37**, 4982–4985 (2010).

18. Ohshita, J., Tada, Y., Kunai, A., Harima, Y. & Kunugi, Y. Hole-injection properties of annealed polythiophene films to replace PEDOT-PSS in multilayered OLED systems. *Synth. Met.* **159**, 214–217 (2009).

19. Hains, A. W. & Marks, T. J. High-efficiency hole extraction/electron-blocking layer to replace poly(3,4-ethylenedioxythiophene):poly(styrene sulfonate) in bulk-heterojunction polymer solar cells. *Appl. Phys. Lett.* **92**, 023504 (2008).

20. Mauger, S. A., Chang, L., Rochester, C. W. & Moulé, A. J. Directional dependence of electron blocking in PEDOT:PSS. *Org. Electron.* **13**, 2747–2756 (2012).

21. So, F. & Kondakov, D. Degradation Mechanisms in Small-Molecule and Polymer Organic Light-Emitting Diodes. *Adv. Mater.* **22**, 3762–3777 (2010).

22. Jørgensen, M., Norrman, K. & Krebs, F. C. Stability/degradation of polymer solar cells. *Solar Energy Materials and Solar Cells* vol. 92 686–714 (2008).

23. De Jong, M. P., Van Ijzendoorn, L. J. & De Voigt, M. J. A. Stability of the interface between indium-tin-oxide and poly(3,4-ethylenedioxythiophene)/poly(styrenesulfonate) in polymer light-emitting diodes. *Appl. Phys. Lett.* **77**, 2255–2257 (2000).

24. Shrotriya, V., Li, G., Yao, Y., Chu, C. W. & Yang, Y. Transition metal oxides as the buffer layer for polymer photovoltaic cells. *Appl. Phys. Lett.* **88**, 073508 (2006).

25. Xu, M. F. *et al.* Aqueous solution-processed MoO3 as an effective interfacial layer in polymer/fullerene based organic solar cells. *Org. Electron.* **14**, 657–664 (2013).

26. Ghasemi Varnamkhasti, M., Fallah, H. R., Mostajaboddavati, M., Ghasemi, R. & Hassanzadeh, A. Comparison of metal oxides as anode buffer layer for small molecule organic photovoltaic cells. *Sol. Energy Mater. Sol. Cells* **98**, 379–384 (2012).

27. Irwin, M. D., Buchholz, D. B., Hains, A. W., Chang, R. P. H. & Marks, T. J. p-Type semiconducting nickel oxide as an efficiency-enhancing anode interfacial layer in polymer bulk-heterojunction solar cells. *Proc. Natl. Acad. Sci. U. S. A.* **105**, 2783–2787 (2008).

28. Intaniwet, A., Keddie, J. L., Shkunov, M. & Sellin, P. J. *High charge-carrier mobilities in blends of poly(triarylamine) and TIPS-pentacene leading to better performing X-ray sensors*. *Organic Electronics* vol. 12 http://epubs.surrey.ac.uk/7284/2/PTAA%2BTIPS-pentacene_paper-Organic-Electronics-Preprint.pdf (2011).

29. Ciavatti, A. *et al.* Toward Low-Voltage and Bendable X-Ray Direct Detectors Based on Organic Semiconducting Single Crystals. *Adv. Mater.* **27**, 7213–7220 (2015).

30. Basirico, L. *et al.* Solid State Organic X-Ray Detectors Based on Rubrene Single Crystals. *IEEE Trans. Nucl. Sci.* **62**, 1791–1797 (2015).

31. Gelinck, G. H. *et al.* X-Ray Detector-on-Plastic with High Sensitivity Using Low Cost, Solution-Processed Organic Photodiodes. *IEEE Trans. Electron Devices* **63**, 197–204 (2016).

32. Kim, Y. C., Choi, Y. S. & Lee, S. Y. Printable organometallic perovskite enables large-area, low-dose X-ray imaging Determination of the key factors that are governing the growth and electronic properties of Perovskite materials View project In-Situ Formed Type I Nanocrystalline Perovskite Film for Highly Efficient Light Emitting Diode View project. (2017) doi:10.1038/nature24032.

33. Shrestha, S. *et al.* High-performance direct conversion X-ray detectors based on sintered hybrid lead triiodide perovskite wafers. *Nat. Photonics* **11**, 436–440 (2017).

34. Gou, Z. *et al.* Self□Powered X□Ray Detector Based on All□Inorganic Perovskite Thick Film with

High Sensitivity Under Low Dose Rate. *Phys. status solidi – Rapid Res. Lett.* **13**, 1900094 (2019).

35. Mescher, H., Hamann, E. & Lemmer, U. Simulation and design of folded perovskite x-ray detectors. *Sci. Rep.* **9**, 1–13 (2019).

36. Yuan, J. *et al.* Enabling low voltage losses and high photocurrent in fullerene-free organic photovoltaics. *Nat. Commun.* **10**, 1–8 (2019).

37. Rahman, M. Y. A., Salleh, M. M., Talib, I. A. & Yahaya, M. Effect of surface roughness of TiO2 films on short-circuit current density of photoelectrochemical cell of ITO/TiO2/ PVC-LiClO4/graphite. *Curr. Appl. Phys.* **5**, 599–602 (2005).

38. Koenigsfeld, N. *et al.* Effect of surface roughness on field emission from chemical vapor deposited polycrystalline diamond. *Appl. Phys. Lett.* **79**, 1288–1290 (2001).

39. Basiricò, L. *et al.* Direct X-ray photoconversion in flexible organic thin film devices operated below 1 V. *Nat. Commun.* **7**, 13063 (2016).

40. Panneerselvam, D. M. & Kabir, M. Z. Evaluation of organic perovskite photoconductors for direct conversion X-ray imaging detectors. *J. Mater. Sci. Mater. Electron.* **28**, 7083–7090 (2017).

41. Liu, J. *et al.* Flexible, Printable Soft-X-Ray Detectors Based on All-Inorganic Perovskite Quantum Dots. *Adv. Mater.* **31**, 1901644 (2019).

42. Glenn F.Knoll. Radiantion Detection and Measurement. in (2010).

43. Kasap, S. O. & Rowlands, J. A. X-ray photoconductors and stabilized a-Se for direct conversion digital flat-panel X-ray image-detectors. *J. Mater. Sci. Mater. Electron.* **11**, 179–198 (2000).

44. Smentkowski, V. S. *et al.* ToF-SIMS depth profiling of organic solar cell layers using an Ar cluster ion source ARTICLES YOU MAY BE INTERESTED IN. *Cite as J. Vac. Sci. Technol. A* **31**, 30601 (2013).

45. Parnell, A. J. *et al.* Depletion of PCBM at the Cathode Interface in P3HT/PCBM Thin Films as Quantified via Neutron Reflectivity Measurements. *Adv. Mater.* **22**, 2444–2447 (2010).

46. Agostinelli, T. *et al.* Real-time investigation of crystallization and phase-segregation dynamics in P3HT:PCBM solar cells during thermal annealing. *Adv. Funct. Mater.* **21**, 1701–1708 (2011).

47. Multilayer formation in spin-coated thin films of low-bandgap polyfluorene:PCBM blends - IOPscience. https://iopscience.iop.org/article/10.1088/0953-8984/17/50/L01.

48. Janovák, L. *et al.* Microstructuration of poly(3-hexylthiophene) leads to bifunctional superhydrophobic and photoreactive surfaces. *Chem. Commun.* **54**, 650–653 (2018).

49. Ma, W., Yang, C., Gong, X., Lee, K. & Heeger, A. J. Thermally Stable, Efficient Polymer Solar Cells with Nanoscale Control of the Interpenetrating Network Morphology. *Adv. Funct. Mater.* **15**, 1617–1622 (2005).

50. Li, G. *et al.* "Solvent Annealing" Effect in Polymer Solar Cells Based on Poly(3-hexylthiophene) and Methanofullerenes. *Adv. Funct. Mater.* **17**, 1636–1644 (2007).

51. Kim, Y. *et al. PHOTOVOLTAIC MATERIALS AND PHENOMENA SCELL-2004 Composition and annealing effects in polythiophene/fullerene solar cells*.

52. Kim, Y. *et al.* A strong regioregularity effect in self-organizing conjugated polymer films and high-efficiency polythiophene:fullerene solar cells. (2006) doi:10.1038/nmat1574.

53. Pivrikas, A., Stadler, P., Neugebauer, H. & Sariciftci, N. S. Substituting the postproduction treatment for bulk-heterojunction solar cells using chemical additives. *Org. Electron.* **9**, 775–782 (2008).

54. Yao, Y., Hou, J., Xu, Z., Li, G. & Yang, Y. Effects of Solvent Mixtures on the Nanoscale Phase Separation in Polymer Solar Cells. *Adv. Funct. Mater.* **18**, 1783–1789 (2008).

55. Als-Nielsen, J. & Mcmorrow, D. *Elements of Modern X-ray Physics Second Edition*.

56. Karagiannidis, P. G., Georgiou, D., Pitsalidis, C., Laskarakis, A. & Logothetidis, S. Evolution of vertical phase separation in P3HT:PCBM thin films induced by thermal annealing. *Mater. Chem. Phys.*

129, 1207–1213 (2011).

57. Chabinyc, M. L. X-ray scattering from films of semiconducting polymers. *Polym. Rev.* **48**, 463–492 (2008).

58. Sirringhaus, H. *et al.* Two-dimensional charge transport in self-organized, high-mobility conjugated polymers. *Nature* **401**, 685–688 (1999).

59. P3HT Revisited – From Molecular Scale to Solar Cell Devices - Google Books. https://books.google.co.uk/books?id=dC9gBQAAQBAJ&pg=PA64&lpg=PA64&dq=is+edge+on+orientation+better+for+charge+transport+than+face-on+for+P3HT&source=bl&ots=c-0xsF_UHe&sig=ACfU3U1jdI15O92xl99Mim3jtSYcFuwn2w&hl=en&sa=X&ved=2ahUKEwih39DmlLvpAhXdQhUIHauaC78Q6AEwAHoECAcQAQ#v=onepage&q=is edge on orientation better for charge transport than face-on for P3HT&f=false.

60. Cullity, B. D. & Stock, S. R. *ELEMENTS OF RAY X-RAY DIFFRACTION*. (ADDISON-WESLEY, 2001).

61. Kočka, J., Arlauskas, K. & Viliūnas, M. Extraction current transients: New method of study of charge transport in microcrystalline silicon. *Phys. Rev. Lett.* **84**, 4946–4949 (2000).

62. Stephen, M., Genevičius, K., Juška, G., Arlauskas, K. & Hiorns, R. C. Charge transport and its characterization using photo-CELIV in bulk heterojunction solar cells. *Polym. Int.* **66**, 13–25 (2017).

63. Kumar, A., Liao, H. H. & Yang, Y. Hole mobility in optimized organic photovoltaic blend films obtained using extraction current transients. *Org. Electron.* **10**, 1615–1620 (2009).

64. Von Hauff, E. Impedance Spectroscopy for Emerging Photovoltaics. (2019) doi:10.1021/acs.jpcc.9b00892.

65. Basham, J. I., Jackson, T. N. & Gundlach, D. J. Predicting the *J* - *V* Curve in Organic Photovoltaics Using Impedance Spectroscopy. *Adv. Energy Mater.* **4**, 1400499 (2014).

66. Boukamp, B. A. A package for impedance/admittance data analysis. *Solid State Ionics* **18–19**, 136–140 (1986).

67. Boukamp, B. A. A Nonlinear Least Squares Fit procedure for analysis of immittance data of electrochemical systems. *Solid State Ionics* **20**, 31–44 (1986).

68. Bisquert, J. Theory of the impedance of electron diffusion and recombination in a thin layer. *J. Phys. Chem. B* **106**, 325–333 (2002).

69. Bange, S., Schubert, M. & Neher, D. Charge mobility determination by current extraction under linear increasing voltages: Case of nonequilibrium charges and field-dependent mobilities. *Phys. Rev. B - Condens. Matter Mater. Phys.* **81**, 035209 (2010).

70. Jansson, P. *Digital Pulse Processing in HPGe Gamma-ray Spectroscopy courses on Activity Measurements with Germanium Detectors*. (2016).

71. Hussein, M., Adams, E. J., Jordan, T. J., Clark, C. H. & Nisbet, A. A critical evaluation of the PTW 2D-ARRAY seven29 and OCTAVIUS II phantom for IMRT and VMAT verification. *J. Appl. Clin. Med. Phys.* **14**, 274–292 (2013).

72. Clark, C. H. *et al.* A multi-institutional dosimetry audit of rotational intensity-modulated radiotherapy. *Radiother. Oncol.* **113**, 272–278 (2014).

73. Webb, S. *Intensity-modulated radiation therapy*. (2015).

74. Bushberg, J. T., Seibert, J. A., Leidholdt, E. M., Boone, J. M. & Goldschmidt, E. J. The Essential Physics of Medical Imaging. *Med. Phys.* **30**, 1936–1936 (2003).

75. Bartoli, A. *et al.* Dosimetric characterization of a 2D polycrystalline CVD diamond detector. in *Journal of Instrumentation* vol. 12 (Institute of Physics Publishing, 2017).

76. Marre, D. & Marinello, G. Comparison of p-type commercial electron diodes for in vivo dosimetry. *Med. Phys.* **31**, 50–56 (2004).

77. Song, H. *et al.* Limitations of silicon diodes for clinical electron dosimetry. *Radiat. Prot. Dosimetry* **120**, 56–59 (2006).

78. Jiang, Z. GIXSGUI: A MATLAB toolbox for grazing-incidence X-ray scattering data visualization and reduction, and indexing of buried three-dimensional periodic nanostructured films. *J. Appl. Crystallogr.* **48**, 917–926 (2015).